Available online at www.sciencedirect.com
SCIENCE DIRECT®
Journal of Membrane Science xxx (2004) xxx–xxx
journal of MEMBRANE SCIENCE
www.elsevier.com/locate/memsci

Direct observation of biofouling in cross-flow microfiltration: mechanisms of deposition and release

Seok-Tae Kang[1], Arun Subramani, Eric M.V. Hoek*, Marc A. Deshusses, Mark R. Matsumoto

Department of Chemical and Environmental Engineering, University of California, Riverside, CA 92521, USA

Received 30 January 2004; received in revised form 2 July 2004; accepted 9 July 2004

Abstract

A laboratory-scale membrane filtration cell was constructed to enable direct microscopic observation of microbial cell deposition and release in cross-flow microfiltration. Initial deposition rates determined from microscopic images were interpreted through an interaction force model. Experimentally derived deposition rates and model calculations confirmed that initial cell and particle deposition was governed by permeation drag and electrostatic double layer forces. Microbial deposition rates increased linearly with increasing permeation velocity over several orders of magnitude, but decreased dramatically with small increases to membrane and particle zeta potential. Cross-flow velocity had no effect on initial deposition up to cross-flow Reynolds numbers of 600. Cell deposition rates were significantly lower at high ionic strength and low pH due to cell aggregation in the bulk. Model equations suggested that cell aggregates were more strongly influenced by tangential shear and lift forces, which tend to reduce deposition. The interaction force model predicted at a set of "critical operating conditions" at which cells were reversibly deposited. Direct observation experiments verified that most cells deposited under the predicted "critical" conditions were easily removed when permeation ceased – without the need for back-pulsing or chemical cleaning. Beyond the fundamental knowledge gained from this study, the experimental and theoretical techniques presented may prove valuable in identifying particle and biological fouling potentials of new membrane materials, as well as in developing effective fouling control strategies for environmental membrane separations.

Keywords: Microfiltration; Ultrafiltration; Fouling; Water treatment; Particle deposition; Biofouling

1. Introduction

Microbial cells attach firmly to almost any surface submerged in an aquatic environment [1]. Immobilized cells grow, reproduce, and produce extra-cellular polymers, which frequently extend from the cell forming a tangled matrix of fibers that provide structure to the assemblage termed a *biofilm* [2]. The generally accepted stages in the development of a biofilm are: initial transport and deposition, more permanent adhesion or release, proliferation and trans-location, and biofilm formation [3]. The unwanted deposition and growth of a biofilm in any system is referred to as *biofouling*. Biofouling is a major problem in environmental membrane separations because it leads to higher operating pressures, more frequent chemical cleanings, shortened membrane life, and compromised product water quality [4–6].

Biofouling is inherently more complicated than other membrane fouling phenomena because microorganisms can grow, multiply, and relocate. Hence, even 99.99% removal of microorganisms from a feed stream can still lead to the eventual formation of a biofilm [7]. Also, the plethora of aquatic microorganisms in existence and their propensity to change surface properties through metabolic processes or environmental stimuli lead to diverse and transient physicochemical properties. Some microorganisms seem inherently "sticky" and tend to rapidly adhere to practically any surface, while others respond more slowly and only adhere to certain sur-

* Corresponding author. Present address: Civil and Environmental Engineering Department, University of California, 5732 Boelter Hall, Los Angeles, CA 90095, USA. Tel.: +1 310 206 3735; fax: +1 310 206 2222.
E-mail address: hoek@seas.ucla.edu (E.M.V. Hoek).
[1] Present address: Department of Environmental Science and Engineering, Kwangju Institute of Science and Technology (KJIST), 1 Oryong-Dong, Buk-Gu, Gwangju, Republic of Korea.

0376-7388/$ – see front matter © 2004 Elsevier B.V. All rights reserved.
doi:10.1016/j.memsci.2004.07.011

faces after some time. Differences in microbial adhesion to surfaces over long times may result from biological factors such as the growth phase and nutritional condition of the microbe, but the initial attachment is largely controlled by physicochemical factors such as solution chemistry, substrate surface properties, and hydrodynamic conditions [1–7].

Several past studies using direct microscopic observation suggested that cross-flow and permeate hydrodynamics control microbial cell and particle deposition onto membranes [8–14], while other studies concluded that solution chemistry and surface properties controlled microbial cell adhesion onto membranes [15–17]. These past studies provide a qualitative understanding that membrane biofouling can be influenced by membrane surface properties (hydrophobicity, charge, roughness, pore size), bulk solution chemistry (pH, ionic strength, and electrolyte type), microbial suspension properties (size, number, and microorganism type), and hydrodynamic factors (permeation, cross-flow, back-pulsing).

The objective of this study was to develop a procedure enabling quantitative determination of the mechanisms governing initial deposition and release of biofoulants in cross-flow microfiltration processes. A laboratory-scale, cross-flow membrane filtration flow cell and direct microscopic observation apparatus similar to that of Mores and Davis [11] was constructed. Yeast cells, bacteria cells, and latex particles served as model microbial particles (i.e., non-motile microorganisms) or "biofoulants". A polysulfone membrane and two modified polyacrylonitrile membranes were tested as model microfiltration membranes. Membrane and particle surface properties were characterized to facilitate modeling of bulk and interfacial transport phenomena, and physicochemical conditions were systematically varied in direct microscopic observation experiments. A novel image analysis procedure enabled rapid quantification of net deposition rates, which were interpreted with the aid of an interaction force balance model.

2. Theory

In cross-flow membrane filtration, the net velocity of microbial particles normal to the membrane surface is largely determined by normal convection with small contributions by tangential convection and Brownian diffusion [18]. Upon close approach, non-specific interfacial forces may dominate bulk transport forces, and thus, govern deposition phenomena [19]. Interfacial forces originate from hydrodynamic, van der Waals, electrostatic double layer, Lewis acid–base, steric, and other physicochemical interactions [19–21]. In dilute electrolytes, electrostatic double layer repulsion is fairly long-ranged and is often the dominant repulsive interfacial force acting to prevent a particle from depositing [19,20].

Cohen and Probstein [22] concluded that colloidal particle deposition onto reverse osmosis membranes was largely determined by particles fluxes attributed to permeate drag and electrostatic double layer repulsion. Wiesner et al. [23] found that permeate convection, tangential lift, shear induced diffusion, Brownian diffusion, and colloidal interactions influenced the accumulation of colloidal and suspended particles to varying degrees. However, the analytical expressions employed in these studies provided order of magnitude estimates of particle fluxes. Subsequently, Song and Elimelech [18] performed rigorous simulations based on numerical solution of the convection–diffusion–migration equation. Their results confirmed that permeation drag and electrostatic double layer repulsion governed particle deposition for small charged particles, while lift and shear forces were more important for large uncharged particles. These seminal studies provided valuable insight into the complex problem of particle deposition in membrane systems, but a facile approach to accurately quantify microbial cell deposition in membrane filtration processes is desirable.

Microbial cell transport by convection and diffusion is reasonably well understood and quantitative analysis is straightforward [3,19,20]. In contrast, cell–substrate interfacial interactions may be quantified through a number of different methods [2,21,24]. In the thermodynamic approach, the interacting surfaces are assumed to physically contact each other under conditions of thermodynamic equilibrium (i.e., reversible adhesion), but this approach does not include an explicit role for electrostatic interactions. The classical Derjaguin, Landau, Verwey, Overbeek (DLVO) theory [25,26] describes interaction energies between two surfaces, based on the sum of London-van der Waals and electrostatic double layer interactions and their decay with separation. More recently, Van Oss [21] introduced an "extended DLVO" (XDLVO) approach, which incorporated short-range Lewis acid–base interactions into the classical DLVO theory.

While there is growing evidence that acid–base interactions are important for colloidal fouling of membranes [27,28], inclusion of acid–base interactions in the XDLVO approach implies that the surface free energies of interacting materials can be accurately characterized. Microbial cell surfaces are both chemically and structurally more complex and heterogeneous than most inert colloid surfaces [1–3], which complicates the characterization of surface energetic properties used in the thermodynamic and XDLVO approaches. Moreover, acid–base surface energies can change dramatically depending on the growth stage of a microorganism, whereas electrokinetic properties are relatively stable [29].

In this study, long-ranged, non-specific DLVO interactions are considered in combination with bulk and interfacial hydrodynamic interactions to describe initial deposition of (non-motile, appendage free) microbial particles onto membrane surfaces. The sum of the bulk and interfacial forces (described below) at a given separation distance provides an estimate of the attractive or repulsive force a microbe or particle might experience. DLVO interactions are modeled from surface area averaged properties of microbes and membranes; therefore, any theoretical prediction of interfacial forces should be considered average and semi-quantitative.

2.1. Permeate drag force

Numerous studies have shown that the drag force on a particle approaching an impermeable surface becomes infinite at small gaps because large pressures develop in the zone of closest approach due to the entrapped liquid film between the particle and wall [20]. The drag force increases as an inverse function of the separation gap and must be modified by an appropriate correction factor. The corrected drag force is usually expressed as

$$F_D = -6\pi\mu_w a_p v_w \phi_H, \quad (1)$$

where ϕ_H (=F/F_∞) is the hydrodynamic correction factor to the Stokes drag force. The negative sign in Eq. (1) indicates the permeate drag force acts normal to and towards the membrane surface. In the vicinity of the membrane surface, it is assumed that the particle velocity is sufficiently small to be ignored and inertial effects are negligible.

Goren [30] derived a theoretical description of the hydrodynamic correction factor for a spherical particle approaching a permeable planar surface that was a complex function of the surface's Darcy permeability, particle size, and separation distance [$\phi_H = f(h/a_p, R_m a_p)$, where h is the separation gap and R_m is the membrane hydraulic resistance, or the inverse of the Darcy permeability]. This correction factor was shown to be larger than 1 at separation distances up to 10 times the particle radius and increased dramatically up to the point of contact, where it was described analytically by $\phi_H = [(2R_m a_p/3) + 1.072^2]^{1/2}$.

Goren [30] provided tabulated results for $\phi_H(h/a_p)$ for a range of $R_m a_p$ values. Although none of the tabulated results exactly fit the conditions tested in this study, we found that the logarithms of tabulated results plotted nearly linearly, which enabled linear interpolation to representative conditions. The interpolated data were then plotted and fit by nonlinear regression to produce modified drag force equations as functions of cell size, membrane hydraulic resistance, and interfacial separation distance. Fitted equations had R^2 values above 95% and produced the analytical "contact" value in every case.

2.2. Gravitational force

The net gravitational force on a cell or particle is determined from the difference between gravitational and buoyant forces, and may be written as

$$F_G = -\tfrac{4}{3}\pi a_p^3 g(\rho_p - \rho_w), \quad (2)$$

where g is the gravitational constant, ρ_w indicates the water density, and ρ_p indicates the particle density. Since most microorganisms are small and their density is not far from that of water, the net gravitational force is negligible.

2.3. Cross-flow lift force

A particle in contact with a planar surface in a channel with laminar cross-flow may experience a lift force due to tangential convection [31]. This force acts normal to and away from the membrane surface and may be described by an equation of the form

$$F_L = 81.2(\rho_w \mu_w \dot{\gamma}_0^3)^{1/2} a_p^3, \quad (3)$$

where $\dot{\gamma}_0$ is the wall shear rate. For a fully developed laminar flow field in a thin rectangular channel, the wall shear rate is given by $\dot{\gamma}_0 = 6Q_f/W_c H_c^2$ (H_c and W_c are the channel height and width, respectively) [32].

2.4. van der Waals force

The attractive van der Waals force between a sphere (particle) and flat plate (membrane) can be calculated from

$$F_A = \frac{-A_H a_p}{6h^2(1 + 5.3(h/\lambda))}, \quad (4)$$

where A_H is the Hamaker constant and λ is a characteristic wavelength (~100 nm) [19]. This expression accounts for retardation effects due to the finite time of propagation of electromagnetic waves traveling between the interacting bodies. The retardation effect significantly reduces the van der Waals force at separations larger than the characteristic wavelength down to about 10 nm of interfacial separation. A Hamaker constant of 1 kT was used for all simulations, based on estimates made from other studies for microorganisms and latex particles interacting with polymeric membranes [28,33,34].

2.5. Electrostatic double layer force

Experimentally determined zeta potentials were substituted for surface potentials to predict repulsive electrostatic double layer forces between particles and membranes. All solution chemistries employed in this study resulted in κa_p values much larger than 100, which implies the range of electrostatic interactions is much smaller than the particle radius. Since the zeta potentials and separation distances considered in model calculations were small ($ze\zeta/kT < 1$ and $h/a_p \ll 1$), the constant surface potential sphere-plate electrical double layer force expression

$$F_R = 2\pi a_p \varepsilon\varepsilon_0 \kappa(\zeta_m^2 + \zeta_p^2) \times \left(\frac{2\zeta_m\zeta_p}{\zeta_m^2 + \zeta_p^2} - e^{-\kappa h}\right)\left(\frac{e^{-\kappa h}}{1 - e^{-2\kappa h}}\right), \quad (5)$$

of Hogg et al. [35] was used. Here ε and ε_0 are the relative permittivity of water and that of vacuum, κ is the inverse Debye length ($\propto I^{1/2}$, I is solution ionic strength), ζ_m and ζ_p are the membrane and particle zeta potentials, and h is the interfacial separation distance.

3. Materials and methods

3.1. Direct observation flow cell and apparatus

A cross-flow membrane filtration (CMF) cell was constructed from polycarbonate with a glass window inserted into the top plate to enable direct microscopic observation of microbial cell and particle deposition. The entire flow cell was mounted on an optical microscope (Olympus BX-51, Japan) stage and 10× microscope objective lens was used to image cells deposited on the membrane surface through the glass window of the flow cell. A CCD camera (5× magnification) mounted on the microscope enabled images to be downloaded in real-time to a laboratory PC for post-processing and image analysis. A schematic illustration of the CMF cell and flow apparatus is presented in Fig. 1.

The dimensions of the cross-flow channel within the flow cell were 1 mm (height, H_c) by 25.4 mm (width, W_c) by 76.2 mm (length, L_c). A double "O-ring" design was used to provide a leak-proof seal at the required operating pressures for the MF membranes tested. A permeate spacer was placed in a shallow insert in the bottom plate, followed by the test membrane and the top plate. The feed suspension was contained in a stainless steel, pressurized feed vessel and the entire system was connected in a closed loop, so that initially the pressure was the same everywhere in the vessel, tubing, and CMF cell.

The feed suspension was circulated through the CMF cell by a peristaltic pump (Master Flex, Cole-Parmer, USA) mounted on the retentate line. Permeation was controlled by a digital peristaltic pump (Master Flex, Cole-Parmer, USA) mounted on the permeate line. Both peristaltic pumps were calibrated across their entire range of flows. Computational fluid dynamic simulations confirmed that a fully developed laminar flow profile was established within the field of view of the microscope [36].

Pressure transducers (Model PX302, Omega Engineering, Stamford, CT) located at the feed, retentate, and permeate ports recorded the corresponding pressures at all times during experiments. Locating the permeate pressure transducer between the flow cell and the permeate pump allowed determination of the actual trans-membrane pressure drop as previously described by Ho and Zydney [37]. Each transducer was calibrated against several pre-calibrated analog pressure gages with pressure metered by a pressurized nitrogen tank to ensure accurate and precise transducer calibration. The transducers were connected to an analog-to-digital converter (Data Logger Pro, Vernier Instruments, Springfield, IL), and the three pressures were downloaded to a laboratory PC in real-time. Extremely steady (i.e., non-pulsing) pressures and flows were maintained within the cross-flow filtration cell because the entire apparatus was connected to the feed pressure vessel through a closed line-loop.

3.2. Model membrane characterization

Commercial polymeric membranes used in this study were designated MX50, MX500, and EW by the manufacturer (GE-Osmonics, Minneatonka, MN). Upon receipt from the manufacturer, residual preservative agents were removed from membrane surfaces by soaking coupons in a 60% alcohol solution for 12 h, followed by 12 h of soaking in deionized water. Soaking in alcohol was repeated and then membranes were stored in deionized water at 5 °C with the water replaced every 2 weeks.

According to the manufacturer, EW is a polysulfone membrane with a relatively hydrophobic surface, whereas the MX membranes were made from polyacrylonitrile (PAN)

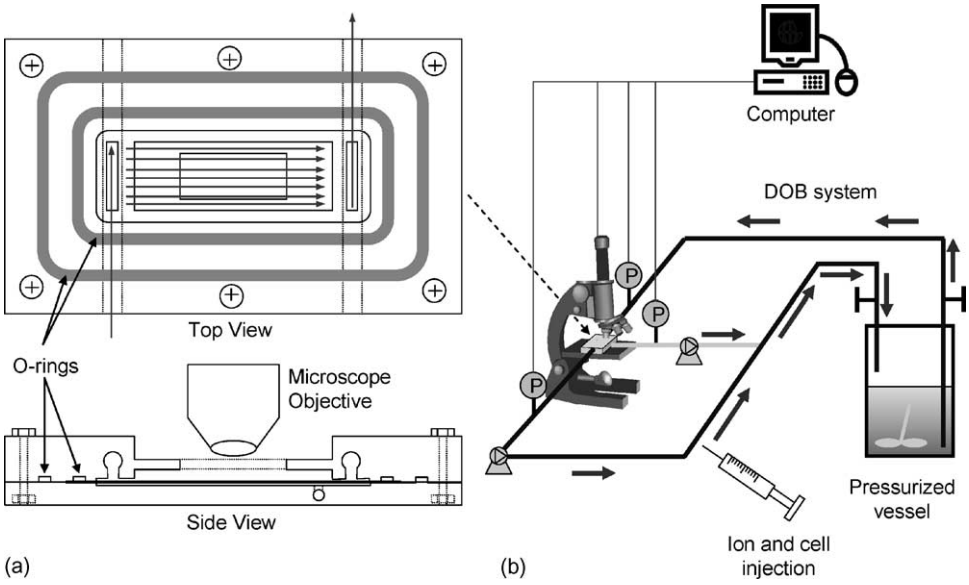

Fig. 1. Schematic diagrams of (a) direct observation flow cell and (b) closed loop filtration system.

and modified to possess a highly hydrophilic surface. The manufacturer rated EW, MX50, and MX500 to have nominal molecular weight cut-offs of approximately 60, 70 and 200 kDa, respectively, at 98% retention of polysaccharides. Hydraulic resistances of membranes were determined by performing a linear regression of pure water flux versus applied pressure data. Membrane surface (zeta) potentials were determined by streaming potential analyzer (EKA, Anton Paar, USA) following previously described methods [38]. Streaming potential was measured on three separate occasions using different membrane coupons.

3.3. Preparation of microbial and particle suspensions

Model biological foulants used in this study were *Saccharomyces cerevisiae* (active dry yeast, Fleischmann, Inc.), *Burkholderia cepacia* G4 (courtesy of Dr. T.K. Wood at the University of Connecticut), and carboxyl-modified latex (CML) particles (Interfacial Dynamics Corporation, USA). Latex particles were supplied by the manufacturer in a 4% (w/v) suspension. The CML particles emitted blue fluorescence at 415 nm (excited at 360 nm), which enabled easy visualization via fluorescence microscopy without modification to the supplied particles. Yeast and bacteria cells were stained to enable visualization via light microscopy.

Before each experiment, 0.26 g of dry *S. cerevisiae* was placed in 100 ml of isotonic water (0.9% NaCl), stirred vigorously for 30 min, and centrifuged at 2000 rpm ($1300 \times g$ for 8 min). The supernatant was removed and the above procedure was repeated three times. A suspension of *B. cepacia* obtained from a pure culture was prepared following the same centrifugation procedure. Centrifuged microbial cells were stained by addition to a solution comprised of 1 ml of 6% Coomassie Brilliant Blue R-250 (Sigma, USA) in 10 ml of acetic acid, 25 ml of isopropanol, and 64 ml of deionized water (final volume of 100 ml). The mixture was stirred for 3 h and then centrifuged. The supernatant was removed and the dyed cells were rinsed twice in deionized water to remove excess dye. The anion of Coomassie Brilliant Blue formed in the acidic staining medium combines with protonated amino groups of proteins through electrostatic interaction [39]. The resulting complex develops intensely colored complexes, but is reversible under the proper conditions. After repeating the washing experiment, the final mass of *S. cerevisiae* was 74 ± 2% of the original mass.

3.4. Model foulant characterization

Surface potentials of model foulants were estimated by measuring electrophoretic mobility (ZetaPALS, Brookhaven Instruments, USA) and converting measured mobilities to zeta potentials by the tabulated data of Ottewill and Shaw [40]. Zeta potentials were measured at a suspension concentration of about 10^5 particles per ml over a range of pH and ionic strengths. Model colloidal foulant sizes were estimated by scanning electron microscopy (SEM) and optical microscopy (OM) with no perceived discrepancy. The hydrodynamic diameter of each model foulant was characterized by a particle size analyzer (Coulter Counter Multisizer, Beckman-Coulter, Inc., USA). The mean of the area in the graph of size and number of particles was taken as the average size. A hemocytometer (grid size 50 μm × 50 μm × 100 μm deep, Fisher Scientific, USA) was used to determine the number concentration of model foulants in each suspension. Cell and particle suspensions were diluted prior to dispensing onto the hemocytometer surface to expedite the manual cell counting procedure. Particle counts of the undiluted suspensions obtained from the Coulter Counter were used to validate the results of the hemocytometer counts.

3.5. Filtration experiment procedure

Membrane coupons were cut from stored samples to fit the flow cell and held in deionized water at room temperature for 30 min prior to insertion in the flow cell. After the membrane was secured in the flow cell, the flow cell was mounted on the microscopic stage and connected to a pressurized vessel containing 2 l of deionized water. Laboratory nitrogen gas was used to maintain pressures up to 345 kPa. After a constant TMP was achieved, permeate flux was consecutively increased and decreased waiting for a stable pressure to be achieved at each flux. Intrinsic membrane resistance was established by performing a linear regression on the pressure versus flux data.

Next, the pressure at experimental flux was maintained steady for at least 10 min and an appropriate volume of premixed stock NaCl solution was injected by syringe through a high-pressure plenum to provide the desired electrolyte concentration. After salt addition, the above procedures were repeated to calculate the membrane resistance to permeation of an electrolyte solution. The apparent membrane resistance changed after adjusting the ionic concentration, suggesting there were significant electro-viscous effects due to the membrane surface charge. Hence, the actual or apparent membrane resistance was used in all model calculations.

Finally, dyed cells or fluorescent latex particles were injected into the pressurized vessel and images of deposited particles were acquired for analysis. The cross-flow and permeation velocities were calculated by dividing the metered feed and permeate flow rates by the cross-sectional area of flow cell and membrane area, respectively. All experiments were conducted between two and six times at each condition. At the end of filtration experiments, the concentration of foulants in the feed vessel was verified using the hemocytometer to determine if there was significant aggregation or changes in particle concentration.

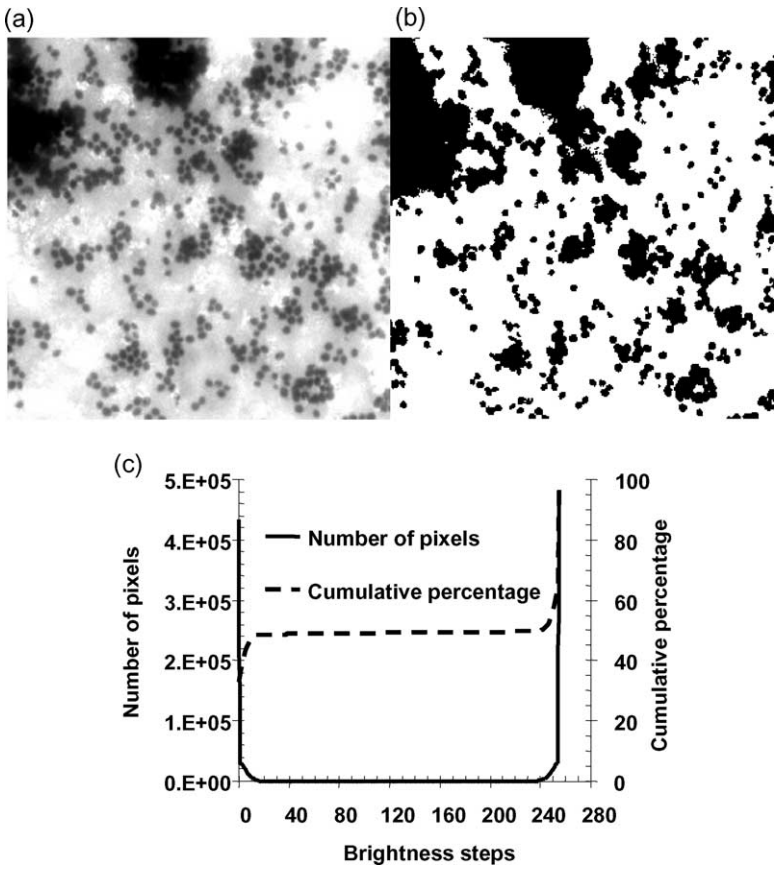

Fig. 2. Determination of fractional surface coverage. Raw grey-scale images (a) acquired through direct microscopic observation were converted into black and white images (b) by choosing an intermediate grey-scale threshold (c). The sums of black and white pixels determine the fractional surface area covered by microbial cells and particles.

3.6. Image acquisition and analysis

High resolution images (1280 × 1024 pixels) acquired through the microscope and CCD camera were downloaded to a laboratory PC and analyzed with NIHs image analysis software (NIH Image J v1.30, downloaded from http://rsb.info.nih.gov/ij/). In a raw grey-scale image, each pixel holds a 256 steps of the integer grey-level value which describes the intensity of the light (0 = black, 255 = white). After selecting an adherent cell found at the same position in consecutive images, a threshold was chosen and the contrast and brightness optimized to obtain the clearest possible image. The distribution of the grey-level was then analyzed to determine the threshold value for conversion of grey-scale images to black and white.

A representative raw grey-scale image, the black and white converted image, and plot of grey-scale intensities are shown in Fig. 2(a)–(c), respectively. Stained microbial particles appeared dark against the white membrane background using standard light microscopy. The inverse analysis was used for fluorescent latex particles, which appeared white with the membrane surface appearing black via fluorescence microscopy. In either case, the converted black and white images were used to determine the fractional coverage by particles at a given time through individual pixel enumeration.

4. Results and discussion

4.1. Physicochemical properties of model biofoulants and membranes

Zeta potentials for *S. cerevisiae* at three different ionic concentrations (0.001, 0.010, and 0.100 M of NaCl) are plotted against pH in Fig. 3(a). The data points are measured values for three experiments and the lines are first order exponential fits to the data. Yeast cell zeta potentials followed expected behavior of decreasing in magnitude with increasing ionic strength and decreasing pH. The cells exhibited an isoelectric point (IEP) at pH 3.0. Fig. 3(b) shows zeta potential at 10 mM NaCl as a function of pH for all three model biofoulants. The latex particles followed a similar trend to the yeast cells, but were more negative at each pH and displayed an IEP of 2.5. Bacteria appeared to have a much lower IEP and the zeta potential change with pH was moderate. So, at neutral pH both microbes had zeta potentials of −21 mV, while the latex zeta potential was

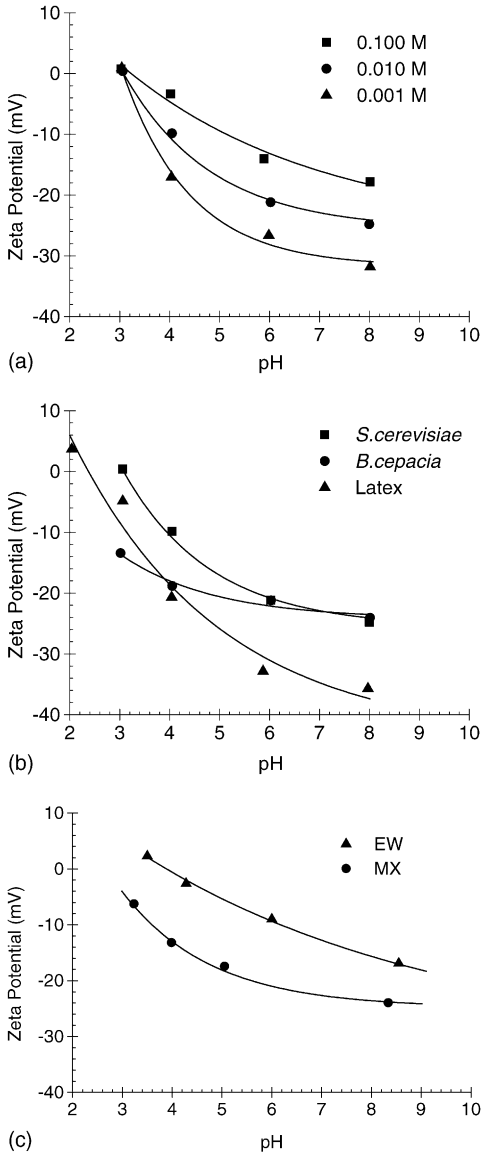

Fig. 3. Zeta potentials of model biofoulants and membranes plotted against solution pH. Zeta potentials for (a) yeast cells at different ionic concentrations and (b) for yeast cells, bacteria cells and latex particles at 0.010 M NaCl. Surface zeta potentials of MX and EW membranes at 0.010 M NaCl vs. pH are plotted in (c).

−35 mV. Zeta potential was determined for both stained and unstained microorganisms with no significant differences between them; hence, the surface charge of the microorganisms was not significantly changed by the dyeing technique. Fig. 3(c) shows the membrane surface (zeta) potentials calculated from streaming potential measurements for the MX and EW membranes. The MX membranes had a more negative zeta potential than EW in the entire range of pH. Average hydraulic resistances of EW, MX50, and MX500 membranes were 5.47×10^9, 1.06×10^9, and 2.98×10^8 Pa s m^{-1}.

4.2. Particle deposition rate constant determination

Preliminary experiments were performed with yeast cells and the MX50 membrane. Constant experimental conditions were permeation velocity 20 μm s^{-1} (40 gfd), cross-flow velocity 25 mm s^{-1}, 10 mM NaCl, pH 5.5, and temperature 20 ± 2 °C, but feed cell concentrations tested were 25, 50, and 100 mg/l. Hereafter, the "standard conditions" will refer to the above experimental conditions at feed cell concentration of 100 mg/l. Direct microscopic images from representative experiments at 30 min of filtration time are provided in Fig. 4 at (a) 25 mg/l, (b) 50 mg/l, and (c) 100 mg/l. The direct microscopic images show increasing extents of surface coverage with increasing feed cell concentration at 30 min of filtration.

Yeast cells appeared to deposit randomly, but some clusters formed on the membrane surface with coverage spreading outward from cluster centers. A small number of yeast cell clusters (comprised of 2–4 primary particles) could be observed in the bulk, indicating some particles were destabilized at the solution chemistry of the experiments, but most cells appeared stable and deposited individually. Occasionally a large cluster would slough off the membrane surface and be washed out of the microscopic field of view, but generally, there was very little rearrangement or re-entrainment after particles initially deposited.

Fractional surface coverage, θ, increased in proportion to the feed cell concentration as shown in Fig. 4(d). Each data point is the average of several experiments at a given time. Surface coverage increased linearly in all experiments up to fractional values of 40–60%, and then tapered off with continued cell deposition. This result should not be confused with a type of "blocking effect" known to decrease particle or molecule adsorption rates as in "random sequential adsorption" [41]. The blocking-like results here were due to the fact that cells depositing on areas already covered by cells did not increase the amount of black area detected through image analysis.

Fractional surface coverage versus time data was then normalized by the number concentration of cells fed into the flow cell and the cross-sectional area of a single particle via

$$N^* = \frac{\theta(t)}{\pi a_p^2 A_m} \frac{1}{N_0}, \tag{6}$$

where A_m is the membrane surface area within the field of view of the microscope objective lens, N_0 the bulk feed cell concentration, and N^* is referred to as the normalized bound cell density (#/m^2). When normalized in this manner, the initial linear slopes of the concentration dependent $\theta(t)$ data collapse into a single slope.

Normalized bound cell density data for all of the concentration variation experiments were plotted up to the point at which the fractional surface coverage data deviated from a constant initial linear growth in Fig. 5(a). The slope describes the concentration independent deposition rate, k_d, which was ∼3 μm s^{-1} for the standard conditions. Since

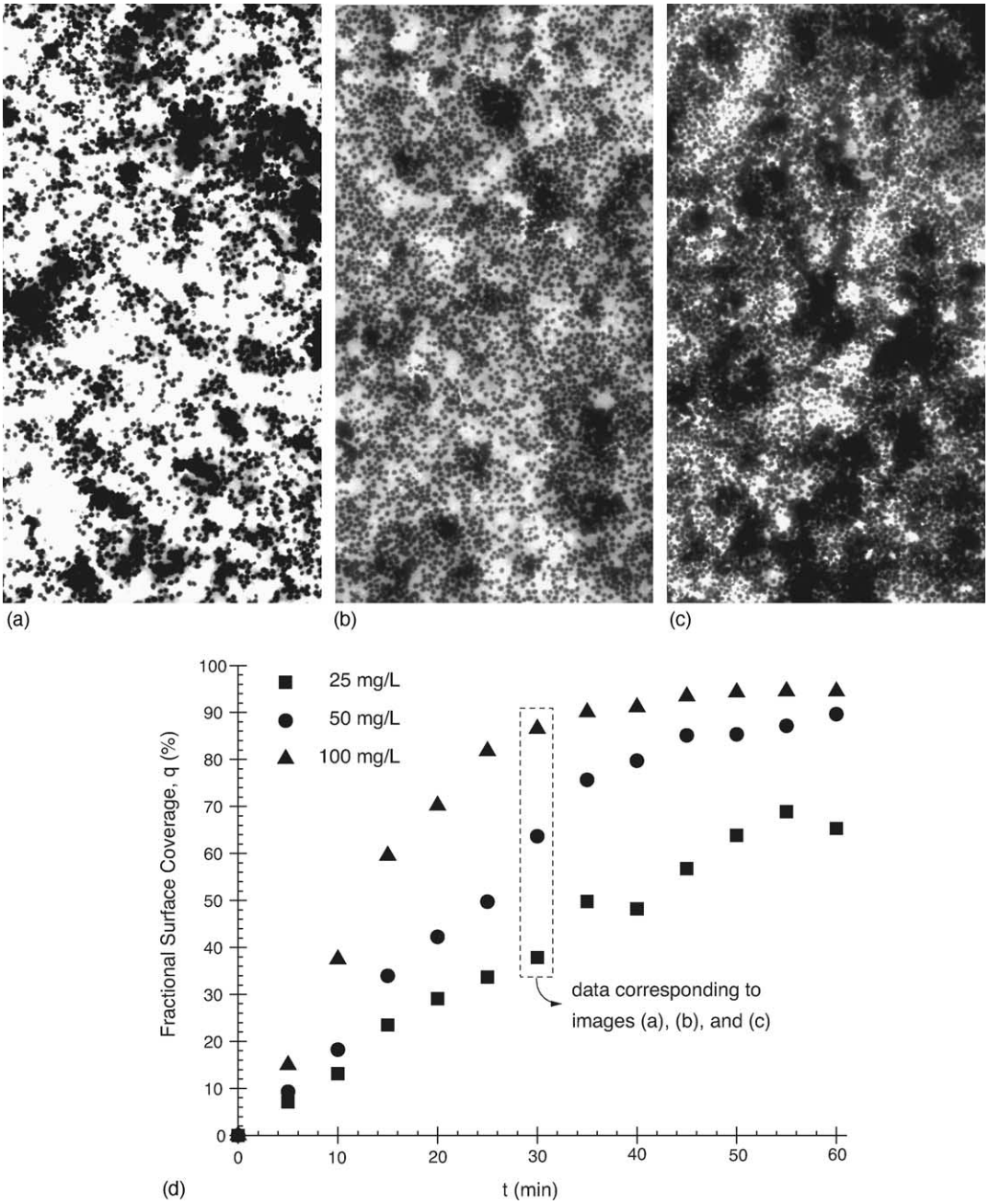

Fig. 4. Direct microscopic images of yeast cells deposited on MX50 membrane after 30 min of filtration at feed cell concentrations of (a) 25 mg/l, (b) 50 mg/l, and (c) 100 mg/l. Fractional surface coverage with time is plotted in (d). Constant experimental conditions employed were permeation velocity 20 $\mu m\,s^{-1}$ (40 gfd), cross-flow velocity 25 $mm\,s^{-1}$ (150 s^{-1}), 10 mM NaCl, pH 5.5 (unadjusted), and temperature 20 ± 2 °C.

there was a small amount of simultaneous deposition and release observed in filtration experiments, k_d should be considered a *net* deposition rate. The interaction forces described in Eqs. (1)–(5) for the experimental conditions were plotted in Fig. 5(b) with the sum of all interaction forces shown as a solid line. None of the interaction forces depend on feed cell concentration, so only one set of interaction force curves was generated for the three experiments. The single total interaction force profile supports the single deposition rate determined experimentally. The net deposition rate constant may be considered the net transport velocity of yeast cells towards the membrane. Multiplying k_d by the feed concentration allows prediction of the actual number of cells depositing per unit area of membrane per unit time.

Cross-flow lift and gravitational forces were negligible for the hydrodynamic conditions simulated. The inset provides a view of the magnitudes of these forces. The DLVO interaction force (dotted line) is negligible up to an interfacial separation of about 20 nm. Strong electrostatic double layer repulsion makes the DLVO interaction completely re-

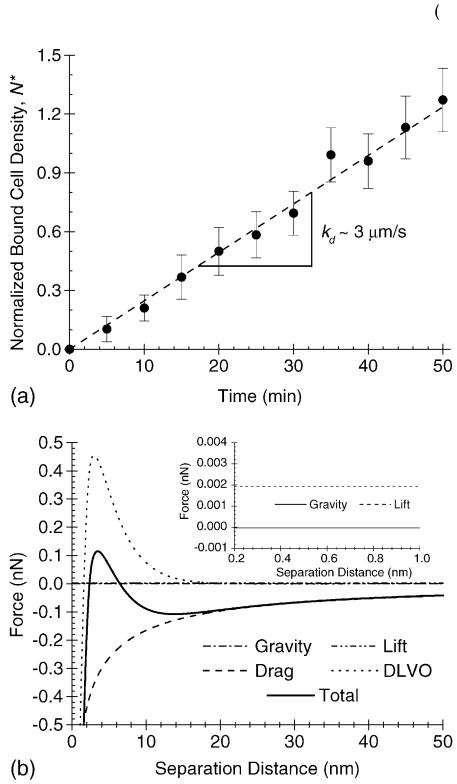

Fig. 5. Influence of yeast cell concentration on (a) normalized bound cell density (N^*) and (b) interaction forces between a yeast cell and MX50 membrane. The slope of N^* vs. time in (a) was the net deposition rate, k_d. Dashed and dotted lines in (b) are individual interaction forces and the solid line is the total interaction force.

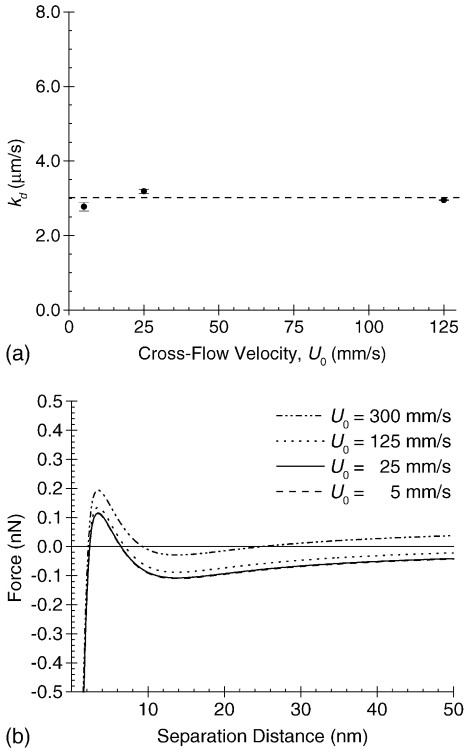

Fig. 6. Influence of cross-flow velocity on (a) net deposition rate and (b) interaction force balance for yeast cells and MX50 membrane. Cross-flow velocities of 5, 25, and 125 mm s^{-1} were tested while all other experimental conditions were same as those described in Fig. 4.

pulsive inside 20 nm up to about 3 nm (the Debye length), at which point van der Waals attraction dominates and the total interaction quickly becomes attractive. Permeation drag (dashed line) is completely attractive and increases in magnitude with decreasing separation. The total interaction force profile (solid line) is attractive at long range, but repulsive inside about 7 nm. The presence of a repulsive (positive) force at close separation does not prohibit particle deposition, as long as an attractive (negative) regime precedes the repulsive barrier.

4.3. Impact of cross-flow velocity on deposition rate

Experiments using yeast cells and MX50 were performed at the standard experimental conditions, but with cross-flow velocities of 5, 25, and 125 mm s^{-1}. The cross-flows tested produced wall shear rates of 30, 150, and 750 s^{-1}, and Reynolds numbers of 10, 50, and 250. Deposition rates at different cross-flow velocities are plotted in Fig. 6(a) with error bars indicating standard deviation at individual cross-flow velocities. The nearly constant net deposition rate confirms that initial particle deposition is independent of bulk cross-flow velocity. Interaction force profiles plotted in Fig. 6(b) were consistent with experimentally derived deposition rates. The forces balanced to zero at a separation distance of 7–10 nm and all force profiles were repulsive at small separations. An additional interaction force profile is shown for a velocity of 300 mm s^{-1}, which was the maximum cross-flow velocity of the experimental system, but a cross-flow velocity of 375 mm s^{-1} ($\dot{\gamma}_0$ = 2250 s^{-1}; Re = 750) would be required to create an entirely repulsive (positive) interaction force curve.

4.4. Impact of permeation velocity on deposition rate

Experiments using yeast cells and MX50 were performed at the standard experimental conditions, but with permeation velocities of 0, 10, 20, and 50 μm s^{-1}, which corresponded to water fluxes 0, 20, 40, and 100 gfd. Data plotted in Fig. 7(a) show a nearly linear increase in k_d as a function of the permeation velocity. The higher deposition rates were attributed primarily to higher rates of transport of cells from the bulk solution to the membrane surface. In addition, the normal drag force on cells approaching the membrane surface increased in proportion to the permeation velocity. The increased drag force is depicted in the interaction force profiles plotted in Fig. 7(b). The model results show an increasingly attractive force profile with increasing permeation velocity, as expected, and completely attractive interactions at the highest permeation velocity.

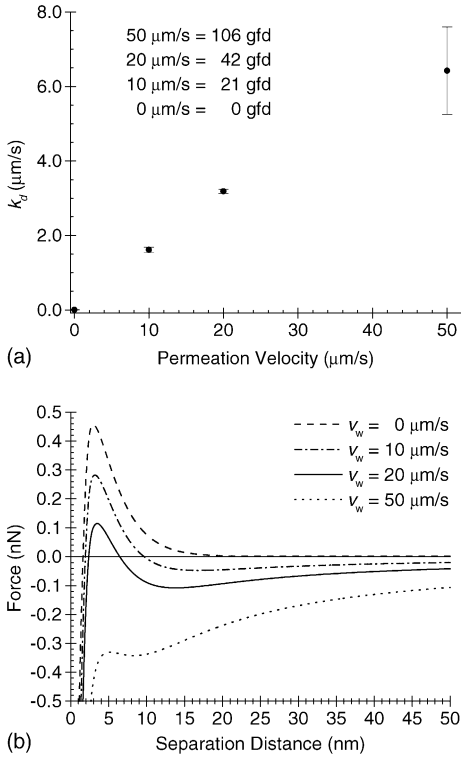

Fig. 7. Influence of permeate velocity on (a) net deposition rate and (b) interaction force balance for yeast cells and MX50 membrane. Permeate velocities of 0, 10, 20, and 50 $\mu m\,s^{-1}$ were tested while all other experimental conditions were same as those described in Fig. 4.

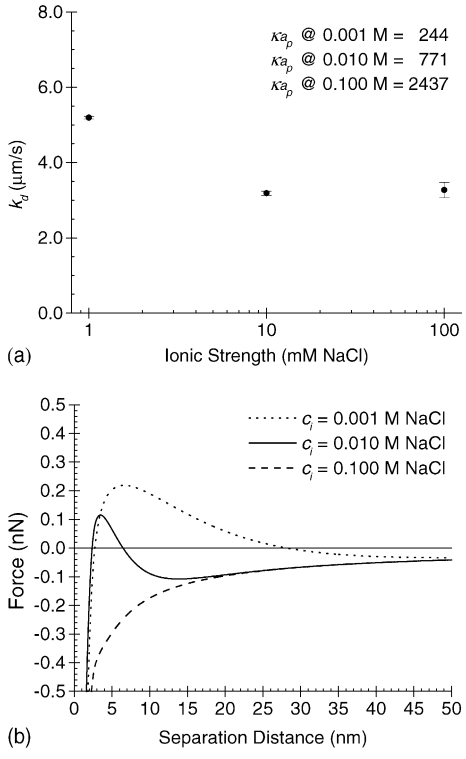

Fig. 8. Influence of ionic concentration on (a) net deposition rate and (b) interaction force balance for yeast cells and MX50 membrane. Ionic concentrations of 1, 10, and 100 mM NaCl were tested while all other experimental conditions were same as those described in Fig. 4.

In absence of permeation, a small, but noticeable, number of cells deposited onto the membrane surface yielding a positive net deposition rate of $\sim 7 \times 10^{-3}\,\mu m\,s^{-1}$. The net positive deposition rate in absence of flux is consistent with particle deposition studies in parallel plate flow cells with impermeable channel walls [2,31,41]. This observation offers a potential explanation for why biofouling cannot be controlled simply by operating at a "critical flux" [42]. The adsorption of a single bacteria to a membrane surface could ultimately lead to biofilm formation and performance decline.

4.5. Impact of solution chemistry on deposition rate

Deposition rates determined for yeast cells and MX50 obtained at the standard experimental conditions, but with ionic concentrations (c_i) of 1, 10, and 100 mM NaCl were plotted in Fig. 8(a). The deposition rates did not vary significantly at 10 and 100 mM, but a dramatically higher deposition rate was determined at 1 mM. The interaction force profiles in Fig. 8(b) suggest an entirely attractive interaction force profile at 100 mM, both attractive and repulsive regimes at 10 mM, and fairly strong and long-ranged repulsion at 1 mM. The lack of agreement between model and experiment may be misleading because at 10 and 100 mM ionic concentrations cells formed small aggregates in the bulk due to double layer compaction. At the lowest ionic concentration, there were no visible aggregates.

A possible explanation emerges from examination of the interaction force balance model equations. The cross-flow lift force scales as a_p^3, the corrected permeation drag force scales as $a_p^{1.5}$, and the DLVO force scales as a_p. As particles grow larger due to aggregation, they should be more strongly affected by the cross-flow lift force and less influenced by permeation and DLVO forces. Therefore, the reduced deposition rates at ionic strengths where aggregates formed were not inconsistent with the functional form of the model equations.

Experiments using yeast cells and MX50 were performed at the standard experimental conditions, but with solution pH of 3.5, 5.5, and 7.5. The deposition rates plotted in Fig. 9(a) were substantially lower at pH 3.5 and 5.5 than at a pH 7.5. The interaction force profiles in Fig. 9(b) suggest an entirely attractive interaction force profile at pH 3.5, both attractive and repulsive regimes at pH 5.5, and fairly strong, but short-ranged repulsion at pH 7.5. At pH 7.5 the particles were stable with no observed aggregation. At pH 3.5 the yeast cells were almost completely destabilized, and considerable aggregation was observed in the bulk. Aggregates were much larger at pH 3.5 than at pH 5.5. Although the larger aggregates should have been more strongly influenced by cross-flow lift at the lowest pH, they were sufficiently destabilized to enable van

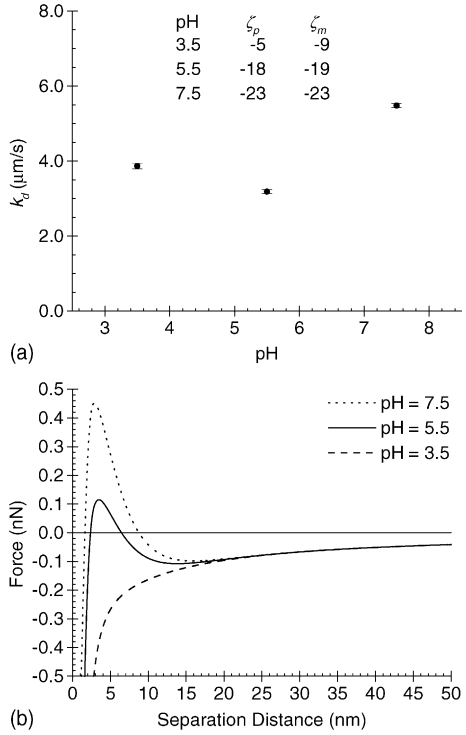

Fig. 9. Influence of pH on (a) net deposition rate and (b) interaction force balance for yeast cells and MX50 membrane. pH values of 3.5, 5.5, and 7.5 were tested while all other experimental conditions were same as those described in Fig. 4.

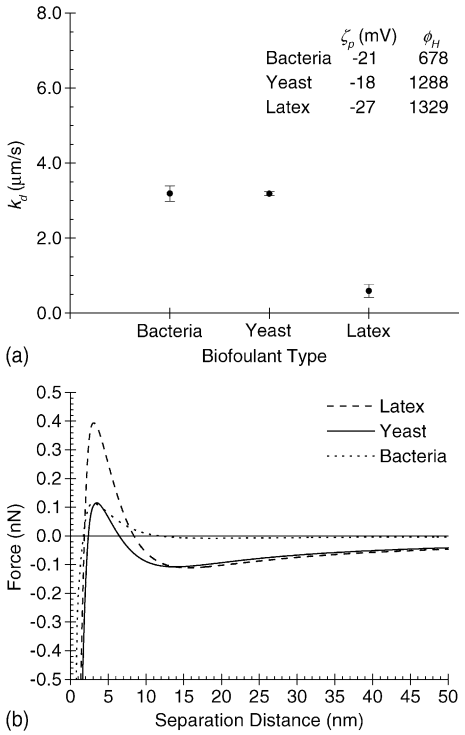

Fig. 10. Influence of cell and particle properties on (a) net deposition rate and (b) interaction force balance for MX50 membrane. *B. cepacia*, *S. cerevisiae*, and carboxylated latex particles were tested while all other experimental conditions were same as those described in Fig. 4.

der Waals attraction to completely overwhelm electrostatic repulsion.

4.6. Impact of biofoulant properties on deposition rate

The deposition rate constants of *S. cerevisiae* (yeast), *B. cepacia* (bacteria), and CML latex particles on MX50 were determined at the standard experimental conditions and plotted in Fig. 10(a). The net deposition rates for the yeast and bacteria cells were not significantly different, but the deposition rate of latex particles was an order of magnitude lower than the microbial particles. Average measured zeta potentials of *S. cerevisiae*, *B. cepacia*, and CML latex at the experimental solution chemistry were -18 ± 2, -21 ± 2, and -27 ± 2 mV, respectively. Average values for the microbes were not statistically different considering the standard experimental error in zeta potential measurement. Interaction force balance profiles for the three particles are plotted in Fig. 10(b). The permeation drag on the bacteria cells was almost half that on the yeast cells and on average the bacteria exhibited a slightly more negative zeta potential. However, the total interaction force profiles predicted almost identical maximum repulsive forces for the two microorganisms. A significantly higher repulsive force was predicted for the latex particles, which was consistent with their lower deposition rate.

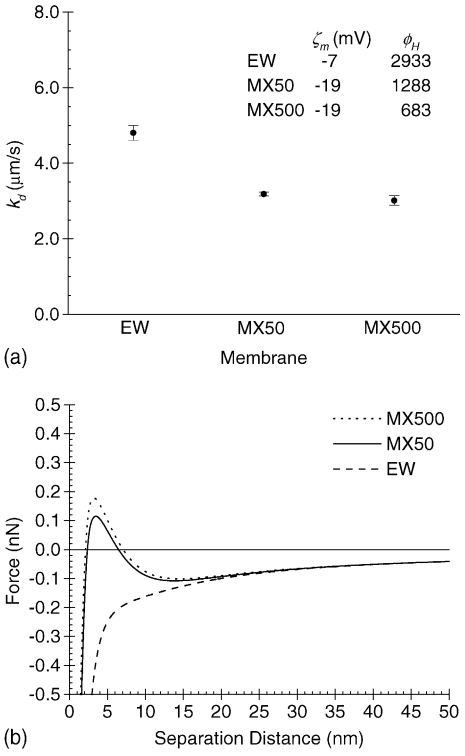

Fig. 11. Influence of membrane surface properties on (a) net deposition rate and (b) interaction force balance for yeast cells. MX500, MX50, and EW membranes were tested while all other experimental conditions were same as those described in Fig. 4.

4.7. Impact of membrane properties on deposition rate

The deposition rate constants of yeast cells on MX50, MX500, and EW were determined at the standard experimental conditions. Net deposition rate constants are shown in Fig. 11(a). The data indicate that the deposition of yeast cells was highest on the EW membrane, and practically identical on MX50 and MX500 membranes. Since the membrane resistances increased in the order of MX500 < MX50 < EW, the influence of permeate drag on particle deposition increases in the same order through the hydrodynamic correction factor, ϕ_H. However, deposition rates appeared more strongly correlated with zeta potential than with the hydrodynamic correction factor. The more negatively charged "hydrophilic" polyacrylonitrile (MX) membranes repeled the yeast cells more strongly than the weakly charged "hydrophobic" polysulfone (EW) membrane.

Interaction force profiles for the three experimental scenarios are plotted in Fig. 11(b). The force profile for EW is completely attractive, whereas the force profiles for MX50 and MX500 show both attractive and repulsive regimes. The modified permeate drag force at contact for MX50 is nearly double that of MX500, but the total interaction force profile upon approach is similar up to very small separations. At the permeation velocity tested, the difference in permeate drag force (arising from differences in membrane hydraulic resistance through the Goren drag correction factor) are relatively small compared to DLVO interactions at small separations.

4.8. Mechanisms of deposition and release

Cells were presumed reversibly deposited under force of permeation drag when a significant electrostatic repulsive barrier was present, such as at the standard experimental conditions. An additional direct observation experiment was performed at the standard conditions using yeast cells and MX50, but with an initial cross-flow velocity of 5 mm s^{-1}. Experimental conditions were maintained constant until the membrane surface was completely covered by yeast cells.

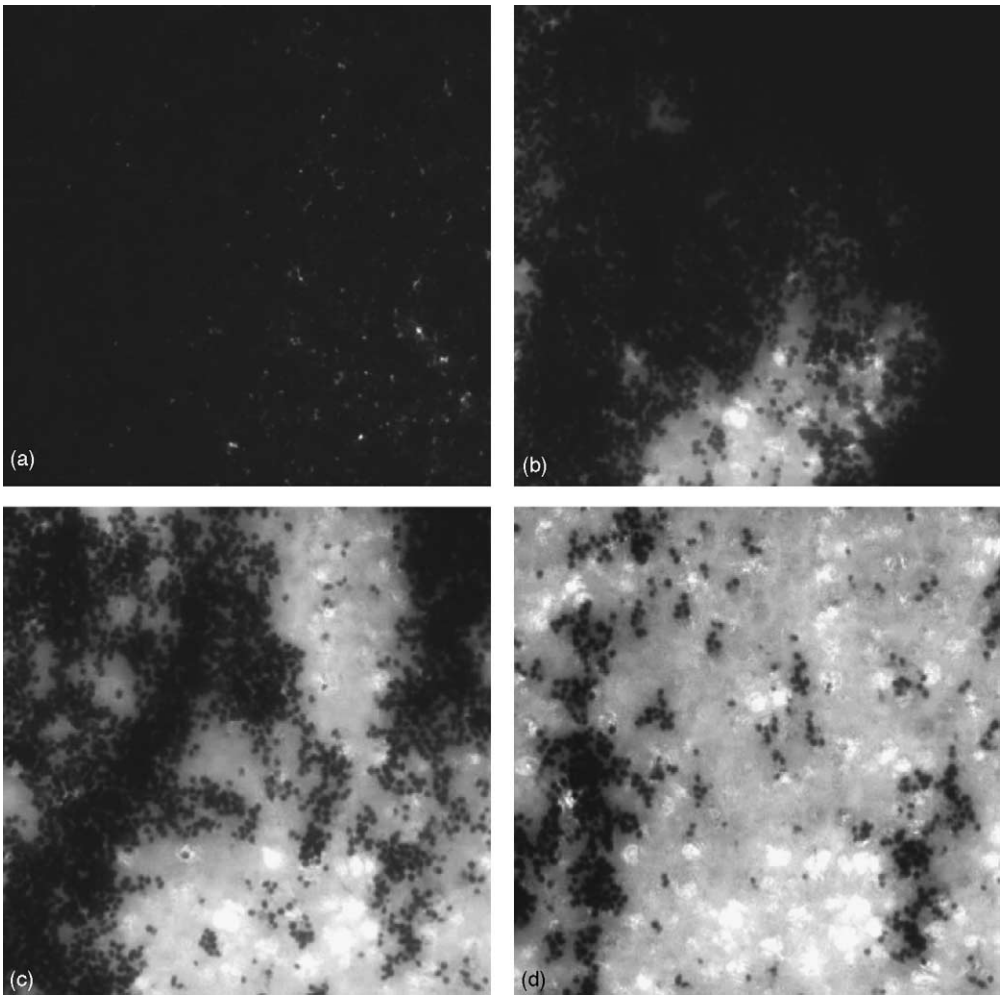

Fig. 12. Optical microscope images of yeast cell deposition and release. Cells were deposited at the standard experimental conditions, except for a cross-flow velocity of 5 mm s^{-1}. Cross-flow velocity was increased to 300 mm s^{-1} with no change in surface coverage as shown in (a). Cells were quickly swept away as observed at (b) 3, (c) 4, and (d) 18 s after permeation ceased.

The cross-flow velocity was then increased in regular increments from 5 mm s^{-1} up to 300 mm s^{-1}, pausing at each cross-flow rate to acquire a microscopic image after 30 s. There was no observable change in yeast cell coverage between the lowest and highest cross-flow velocities, which confirmed the relative insignificance of cross-flow hydrodynamics up to a Reynolds number of 600. Fig. 12(a) is an image taken after the velocity was raised to 300 mm s^{-1}. The force profiles in Fig. 6(b) describe interaction forces for the conditions tested up to this point. The presence of repulsive forces at small cell-membrane separations suggested that on average cells were held near the membrane surface by permeation drag, but were not in physical contact with the membrane surface (i.e., reversible deposition).

Next, the permeate pump was turned off instantly stopping permeation and the deposited cells were rapidly swept away from the membrane surface. Images in Fig. 12(b)–(d) were taken at 3, 4, and 18 s after permeation ceased. At 18 s the fractional surface coverage was about 10%. The interaction force profile for 0 μm s^{-1} permeation velocity in Fig. 7(b) represents the no flux scenario for the standard conditions. Although the interaction force balance profile was completely repulsive, 100% removal was not achieved at longer times.

The natural variation in cell and membrane surface properties could explain the deposition of cells onto membrane surfaces that are on average repulsive. In addition, nanometer scale surface roughness of polymeric membranes has been shown to dramatically reduce the range and magnitude of DLVO interactions and create a distribution of interaction profiles – even if the surface is chemically uniform [43]. Alternatively, chemical heterogeneities on cell and membrane surfaces may create localized sites where interfacial forces are attractive and deposition is favorable. However, these non-idealities in combination with short-range acid–base interactions appear to have a subtle effect on yeast cell deposition onto these membranes.

5. Conclusions

Net deposition rates derived from direct microscopic observation experiments were combined with an interaction force balance model to elucidate the key physicochemical parameters governing microbial cell and latex particle deposition onto polymeric microfiltration membranes. Initial deposition of cells and particles was predominantly controlled by electrostatic double layer repulsion and permeation drag. The more negative zeta potentials of the modified polyacrylonitrile membranes resulted in significantly lower yeast cell deposition than on a weakly charged polysulfone membrane. Yeast and bacteria cells deposited nearly an order of magnitude faster than carboxyl-modified latex particles; the difference was attributed to the more negative zeta potential of the latex particles. Cross-flow hydrodynamics did not affect yeast cell deposition up to a Reynolds number of 600. Lowering solution pH or increasing ionic strength destabilized cells, causing aggregation in the bulk, and both resulted in lower net deposition rates of yeast cells. This unexpected result suggests pre-coagulation of particle suspensions may hinder deposition, as well as produce more porous cake layers [23].

The interaction force model predicted the dominant interaction forces governing particle deposition to be permeation drag and electrostatic repulsion, and total interaction force profiles agreed qualitatively with observed net deposition rates. A set of "critical conditions" predicted by the interaction force model were verified experimentally, providing evidence that cells were reversibly held near the membrane–solution interface under force of permeation drag. Beyond the fundamental knowledge gained, the direct observation system and image analysis procedure provides a quantitative and realistic assessment of membrane fouling potential. The direct observation technique may prove valuable for anyone interested in rapidly identifying fouling potentials of membrane materials, optimizing operating conditions, and developing improved cleaning strategies for environmental membrane separations.

Acknowledgements

Partial support for this work was provided by a post-doctoral fellowship to support Dr. Seok-Tae Kang obtained from the Korea Science and Engineering Foundation (KOSEF). Additional support was obtained from the United States Environmental Protection Agency (US EPA) through the Desalination Research Innovation Partnership (DRIP), which is managed by the Metropolitan Water District of Southern California.

Nomenclature

a_p	particle/cell radius (m)
A_H	Hamaker constant (J)
A_m	membrane surface area (m^2)
c_i	salt concentration (mol l^{-1})
F	drag force at fluid–membrane interface (N)
F_A	van der Waals force (N)
F_D	permeate drag force (N)
F_G	net gravitational force (N)
F_L	cross-flow lift force (N)
F_R	electrostatic double layer force (N)
F_∞	drag force in bulk of fluid (N)
g	gravitational constant (9.81 m s^{-2})
h	interfacial separation distance (m)
h_c	half channel height, $=H_c/2$ (m)
H_c	channel height (m)
I	solution ionic strength, $=1/2 \sum c_i z_i^2$ (mol l^{-1})
k	Boltzmann's constant, 1.3807×10^{-23} (J K^{-1})

k_d	deposition rate constant ($\mu m\,s^{-1}$)
L_c	channel length (m)
N_0	bulk cell/particle number concentration ($\#\,m\,l^{-1}$)
N^*	normalized bound cell density (m)
Q_f	volumetric feed flow rate ($ml\,min^{-1}$)
Q_p	volumetric permeate flow rate ($ml\,min^{-1}$)
R_m	intrinsic membrane hydraulic resistance (m^{-1})
Re	cross-flow Reynolds number, $= 2\rho_w U_0 H_c \mu_w^{-1}$
t	time (s)
T	absolute temperature (K)
U_0	channel average cross-flow velocity ($m\,s^{-1}$)
v_w	permeate water velocity or flux ($m\,s^{-1}$)
W_c	channel width (m)
z_i	ionic valence

Greek letters

$\dot{\gamma}_0$	wall shear rate, $= 6Q_f W_c^{-1} H_c^{-1}$ (s^{-1})
ε	relative permittivity of water, 78.4
ε_0	permittivity of vacuum, 8.85×10^{-12} ($C^2\,J^{-1}\,m^{-1}$)
ζ_m	membrane surface (zeta) potential (mV)
ζ_p	particle/cell surface (zeta) potential (mV)
θ	fractional surface coverage on the membrane
κ	inverse Debye length, $=3.28 \times 10^9 I^{1/2}$ (m^{-1})
λ	characteristic wavelength, 100 nm (m^{-1})
μ_w	dynamic water viscosity ($kg\,m^{-1}\,s^{-1}$)
ρ_p	particle/cell density ($kg\,m^{-3}$)
ρ_w	water density ($kg\,m^{-3}$)
ϕ_H	hydrodynamic correction factor, $=F/F_\infty$

References

[1] J. Wimpenny, Structural determinants in biofilm formation, in: L.V. Evans (Ed.), Biofilms: Recent Advances in their Study and Control, Harwood Academic Publishers, Amsterdam, NL, 2000, 466 pp.
[2] R. Bos, H.C. Van Der Mei, H.J. Busscher, Physico-chemistry of initial microbial adhesive interactions – its mechanisms and methods for study, FEMS Microbiol. Rev. 23 (1999) 179.
[3] W.G. Characklis, K.C. Marshall, Biofilms, Wiley, New York, 1990.
[4] M. Al-Ahmad, F.A.A. Aleem, A. Mutiri, A. Ubaisy, Biofuoling in RO membrane systems. Part 1. Fundamentals and control, Desalination 132 (2000) 173.
[5] J.S. Baker, L.Y. Dudley, Biofouling in membrane systems – a review, Desalination 118 (1998) 81.
[6] H.C. Flemming, Biofouling in water systems – cases, causes and countermeasures, Appl. Microbiol. Biotechnol. 59 (2002) 629.
[7] H.C. Flemming, G. Schaule, T. Griebe, J. Schmitt, A. Tamachkiarowa, Biofouling – the Achilles heel of membrane processes, Desalination 113 (1997) 215.
[8] H. Li, A.G. Fane, H.G.L. Coster, S. Vigneswaran, Direct observation of particle deposition on the membrane surface during crossflow microfiltration, J. Membr. Sci. 149 (1998) 83.
[9] H. Li, A.G. Fane, H.G.L. Coster, S. Vigneswaran, An assessment of depolarisation models of crossflow microfiltration by direct observation through the membrane, J. Membr. Sci. 172 (2000) 135.
[10] H. Li, A.G. Fane, H.G.L. Coster, S. Vigneswaran, Observation of deposition and removal behaviour of submicron bacteria on the membrane surface during crossflow microfiltration, J. Membr. Sci. 217 (2003) 29.
[11] W.D. Mores, R.H. Davis, Direct visual observation of yeast deposition and removal during microfiltration, J. Membr. Sci. 189 (2001) 217.
[12] W.D. Mores, R.H. Davis, Yeast foulant removal by backpulses in crossflow microfiltration, J. Membr. Sci. 208 (2002) 389.
[13] W.D. Mores, R.H. Davis, Direct observation of membrane cleaning via rapid backpulsing, Desalination 146 (2002) 135.
[14] W.D. Mores, R.H. Davis, Yeast-fouling effects in cross-flow microfiltration with periodic reverse filtration, Ind. Eng. Chem. Res. 42 (2003) 130.
[15] S.B.S. Ghayeni, P.J. Beatson, R.P. Schneider, A.G. Fane, Adhesion of waste water bacteria to reverse osmosis membranes, J. Membr. Sci. 138 (1998) 29.
[16] T. Knoell, J. Safarik, T. Cormack, R. Riley, S.W. Lin, H. Ridgway, Biofouling potentials of microporous polysulfone membranes containing a sulfonated polyether-ethersulfone/polyethersulfone block copolymer: correlation of membrane surface properties with bacterial attachment, J. Membr. Sci. 157 (1999) 117.
[17] P. Campbell, R. Srinivasan, T. Knoell, D. Phipps, K. Ishida, J. Safarik, T. Cormack, H. Ridgway, Quantitative structure–activity relationship (QSAR) analysis of surfactants influencing attachment of a *Mycobacterium* sp. to cellulose acetate and aromatic polyamide reverse osmosis membranes, Biotechnol. Bioeng. 64 (1999) 527.
[18] L.F. Song, M. Elimelech, Particle deposition onto a permeable surface in laminar-flow, J. Colloid Interf. Sci. 173 (1995) 165.
[19] M. Elimelech, J. Gregory, X. Jia, R.A. Williams, Particle Deposition and Aggregation: Measurement, Modeling and Simulation, Butterworths–Heinemann, Woburn, MA, 1995.
[20] R.F. Probstein, Physicochemical Hydrodynamics, 2nd ed., Wiley, New York, NY, 1994.
[21] C.J. Van Oss, Interfacial Forces in Aqueous Media, Marcel Dekker, New York, NY, 1994.
[22] R.D. Cohen, R.F. Probstein, Colloidal fouling of reverse osmosis membranes, J. Colloid Interf. Sci. 114 (1986) 194.
[23] M.R. Wiesner, M.M. Clark, J. Mallevialle, Membrane filtration of coagulated suspensions, J. Environ. Eng.-ASCE 115 (1989) 20.
[24] J.N. Israelachvili, Intermolecular and Surface Forces, 2nd ed., Academic Press, London, 1992.
[25] B.V. Derjaguin, L.D. Landau, Theory of the stability of strongly charged lyophobic sols and of the adhesion of strongly charged particles in solutions of electrolytes, Acta Physicochim. URSS 14 (1941) 733.
[26] E.J.W. Verwey, J.T.G. Overbeek, Theory of the Stability of Lyophobic Colloids, Elsevier, Amsterdam, 1948.
[27] J.A. Brant, A.E. Childress, Membrane–colloid interactions: comparison of extended DLVO predictions with AFM force measurements, Environ. Eng. Sci. 19 (2002) 413.
[28] J.A. Brant, A.E. Childress, Assessing short-range membrane–colloid interactions using surface energetics, J. Membr. Sci. 203 (2002) 257.
[29] D. Grasso, K. Subramaniam, M. Butkus, K. Strevett, J. Bergendahl, A review of non-DLVO interactions in environmental colloidal systems, Rev. Environ. Sci. Biotech. 1 (2002) 17.
[30] S.L. Goren, The hydrodynamic force resisting the approach of a sphere to a plane permeable wall, J. Colloid Interf. Sci. 69 (1973) 78.
[31] J.N. Ryan, M. Elimelech, Colloid mobilization and transport in groundwater, Colloid Surf. A: Physicochem. Eng. Asp. 107 (1996) 1.
[32] R.H. Davis, Modeling of fouling of cross-flow microfiltration membranes, Sep. Purif. Meth. 21 (1992) 75.
[33] G. Chen, K.A. Strevett, Impact of surface thermodynamics on bacterial transport, Environ. Microbiol. 3 (2001) 237.

[34] P.K. Sharma, K.H. Rao, Analysis of different approaches for evaluation of surface energy of microbial cells by contact angle goniometry, Adv. Colloid Interface Sci. 98 (2002) 341.
[35] R.I. Hogg, T.W. Healy, D.W. Fuerstenau, Mutual coagulation of colloidal dispersions, Trans. Faraday Soc. 62 (1966) 1638.
[36] S.-T. Kang, A. Subramani, E.M.V. Hoek, M.A. Deshusses, M.D. Matsumoto, Measuring initial microbial adhesion rates on membrane surfaces, American Institute of Chemical Engineers Annual Meeting, San Francisco, CA, 2003.
[37] C.C. Ho, A.L. Zydney, Transmembrane pressure profiles during constant flux. Microfiltration of bovine serum albumin, J. Membr. Sci. 209 (2002) 363.
[38] S.L. Walker, S. Bhattacharjee, E.M.V. Hoek, M. Elimelech, A novel asymmetric clamping cell for measuring streaming potential of flat surfaces, Langmuir 18 (2002) 2193.
[39] I. Syrovy, Z. Hodny, Staining and quantification of proteins separated by polyacrylamide-gel electrophoresis, J. Chromatogr.-Biomed. Appl. 569 (1991) 175.
[40] R.H. Ottewill, J.N. Shaw, Electrophoretic studies on polystyrene lattices, J. Electroanal. Chem. 37 (1972) 133.
[41] Z. Adamczyk, P. Belouschek, Localized adsorption of particles on spherical and cylindrical interfaces, J. Colloid Interf. Sci. 146 (1991) 123.
[42] R.W. Field, D. Wu, J.A. Howell, B.B. Gupta, Critical flux concept for microfiltration fouling, J. Membr. Sci. 100 (1995) 259.
[43] E.M.V. Hoek, S. Bhattacharjee, M. Elimelech, Effect of membrane surface roughness on colloid-membrane DLVO interactions, Langmuir 19 (2003) 4836.